ADVANCED ENERGY MATERIALS
www.advenergymat.de

# Stable Cycling of Mg Metal Anodes by Regulating the Reactivity of $Mg^{2+}$ Solvation Species

*Zheng Li, Dan-Thien Nguyen, J. David Bazak, Kee Sung Han, Ying Chen, Venkateshkumar Prabhakaran, Thuy Thanh Le, Zezhen Cheng, Minyung Song, Vilas G. Pol, Karl T. Mueller, and Vijayakumar Murugesan**

**Rationally designing stable nonaqueous electrolytes for Mg metal anodes demands a thorough understanding of their interfacial behaviors. Here, the critical role of cation–anion pairing in improving the cathodic stabilities of amine-based electrolytes against solvent reduction and $H_2$ evolution is identified. It is demonstrated that strong coordination between solvating amine groups and the $Mg^{2+}$ cation facilitates the dehydrogenation of the $-NH_2$ group, which is mainly responsible for low reversibility during Mg metal plating and stripping. Introducing ion-pairing into the primary solvation shell can effectively weaken the amine coordination such that its reduction is suppressed. A novel interfacial behavior regarding parasitic reaction product dissolution is also identified, which is responsible for the failure of interfacial passivation. An ion-pairing electrolyte is developed based on a weakly-solvated amine molecule and strongly coordinating $Mg^{2+}$ salt. This electrolyte composition delivers long-term Mg metal anode cycling with 99.6% Coulombic efficiency for 800 cycles.**

## 1. Introduction

The increasing demand for large-scale, lower-cost energy storage systems requires the development of next-generation secondary batteries that can equal or eclipse the great success of Li-ion batteries. Multivalent batteries such as rechargeable magnesium (Mg) batteries (RMBs) are promising candidates due to the earth-abundance and low cost of the raw materials and the potential for high volumetric energy density.[1–3] However, developing suitable electrolytes for RMBs is distinctly challenging owing to the large charge density from $Mg^{2+}$ combined with the highly reductive Mg metal anode.[4,5] The charge density of the $Mg^{2+}$ cation enables tight coordination to conventional nonaqueous solvents such as ethers and carbonates, which causes dramatic difficulties for the interfacial desolvation and charge transfer steps of the electrochemical cycling process.[6,7] These issues can lead to large overpotentials during Mg anode cycling and undesired parasitic reactions.[8–10] Highly reactive Mg metal can easily reduce the solvents as well as the anions, generating a solid electrolyte interphase (SEI) layer which generally prevents the diffusion of $Mg^{2+}$ to the electrode, thereby blocking the subsequent reduction process at the metallic surface.[11–13] Consequently, developing a suitable electrolyte that enables facile interfacial charge transfer, high reduction stability, and favorable SEI formation are prerequisites for the stable long-term cycling of RMBs.[14] However, the development of rational electrolyte design principles for RMBs is hindered by a lack of fundamental understanding of the interfacial behaviors and stabilities of the electrolyte solvation structures.[2]

Recently, correlations between the Mg plating–striping overpotential and the electrolytes' interfacial charge transfer behavior have been well demonstrated. Notably, a family of amine-based electrolytes that feature easier solvation shell reorganization and desolvation processes were identified to decrease the interfacial charge transfer energy barriers. The overpotential of Mg plating–stripping was dramatically reduced compared to that in the conventional ether-based electrolytes.[15,16] However, the reversibility of Mg plating–stripping relied on several factors such as the charge transfer mechanism, the morphology of Mg deposition, decomposition mechanism of electrolyte, and the stability of the SEI. For example, the reported amine-based electrolytes with 2-methoxyethylamine (MEA) and 3-methoxypropylamine (MPA)

Z. Li, D.-T. Nguyen, J. D. Bazak, K. S. Han, Y. Chen, V. Prabhakaran, M. Song, K. T. Mueller, V. Murugesan
The Joint Center for Energy Storage Research
Pacific Northwest National Laboratory
Richland, WA 99352, USA
E-mail: vijay@pnnl.gov
Z. Li, V. G. Pol
Davidson School of Chemical Engineering
Purdue University
West Lafayette, IN 47907, USA
D.-T. Nguyen, J. D. Bazak, K. S. Han, Y. Chen, V. Prabhakaran, T. T. Le, Z. Cheng, M. Song, K. T. Mueller, V. Murugesan
Pacific Northwest National Laboratory
Richland, WA 99352, USA
The ORCID identification number(s) for the author(s) of this article can be found under https://doi.org/10.1002/aenm.202301544



**DOI: 10.1002/aenm.202301544**

solvents by Wang et al. exhibited a dramatic Coulombic efficiency (CE) difference (≈65% vs 95.5%) but nevertheless similarly low overpotential, below 100 mV.[16] Therefore, the parasitic reactions that occur to decrease the anode efficiency are subject to other yet unknown factors, such as the decomposition of MEA and MPA and its signature on the SEI composition. The intrinsic cathodic stabilities of the diverse solvation structures originating from different ion coordination environments have been somewhat overlooked. The SEI evolution and its dependence on the electrolyte solvation structures were also not robustly interpreted.

Here, we report a detailed, molecular-level investigation of the solvation structures of amine-based electrolytes and their interfacial reactivities with Mg metal anode. We selected a series of amine-based electrolytes with various degrees of ion pair formation designed to systematically explore the influence of solvent and salt coordination on electrochemical performance. It is demonstrated that the fully solvent-separated ion pair (SSIP) is prone to reduction at the anode interface, while strategically introducing a suitable anion into the solvation structure can increase stability and lead to high anode efficiency. We further characterized the interfacial reduction behaviors of the electrolytes by tracking the SEI accumulation and product dissolution to identify their reaction pathways and interpret the cell failure mechanisms. Finally, we performed density functional theory (DFT) calculations to understand the solvation and ion pair energetics and trace the influence of incorporating anions in the solvation shell on the vulnerable N—H bonds in Mg-coordinated amine solvents.

## 2. Results

In this work, methoxy-amine-based electrolytes were studied as model systems. The MEA solvent combined with the $Mg(TFSI)_2$ salt (denoted as MEA-TFSI) was selected as the baseline electrolyte while replacing the $Mg(TFSI)_2$ with $Mg(OTF)_2$ (denoted as MEA-OTF) was expected to introduce ion pairs into the electrolyte due to the stronger Mg-OTF coordination.[17] Further changing the MEA solvent to MPA, which has less solvation stability, was intended to enrich the ion-paring species (and is denoted as MPA-OTF). These three electrolyte compositions together yield a series with gradually diminishing salt dissociation and commensurately strengthening cation–anion interactions, furnishing an ideal test bed to assess how interfacial behaviors on the Mg metal anode can be regulated by tuning of the $Mg^{2+}$ solvation structure. Here the salt concentration of all studied electrolytes was fixed to 0.1 M for a consistent comparison study, as that is the maximum solubility of $Mg(OTF)_2$ in the MPA solvent.

As a baseline for comparisons, the solvation structures of the three electrolytes were determined via multimodal spectroscopic characterizations, as illustrated in **Figure 1**. Raman spectroscopy (Figure 1a) reveals the ion interactions, with the S—N—S stretching vibration for the $TFSI^-$ anion[15] (720 to 760 $cm^{-1}$) and the S—O stretching vibration for the $OTF^-$ anion[18,19] (1010 to 1050 $cm^{-1}$) reflecting the corresponding degrees of salt dissociation. The strong solvation ability of MEA coupled with the high charge stability of the $TFSI^-$ anion induces full dissociation of the $Mg(TFSI)_2$ salt, such that only a single peak from the free $TFSI^-$ anion can be observed. However, stronger coordination between $Mg^{2+}$ and $OTF^-$ generates contact ion pairs (CIPs) with both the MEA and MPA solvents, with the MPA-OTF electrolyte possessing the highest CIP concentration of the compositions studied here. Fourier-transform infrared spectroscopy (FTIR) analyses were also performed to confirm the nature of the $Mg^{2+}$ cation coordination with the solvent molecules. As shown in Figure 1b, the stretching vibration peaks of the C—O bonds from the solvent molecules between 1000 and 1350 $cm^{-1}$ were collected and compared. Dissolving $Mg(OTF)_2$ salt into MPA resulted in negligible peak changes below 1150 $cm^{-1}$, indicating that there is minimal $Mg^{2+}$ coordination to the O atom and thus primarily monodentate solvent coordination behavior by the $NH_2$ group. Due to the shorter chain length, MEA can induce bidentate coordination to the $Mg^{2+}$ which generates a new peak (or shoulder) at 1060 $cm^{-1}$. Moreover, the characteristic peaks of ion-paired $Mg(OTF)_2$ salt were identified at 1313 and 1245 cm,$^{-1}$[20] which corroborated the Raman results. The FTIR signals from the $NH_2$-vibration range (at ≈ 2800 $cm^{-1}$) in Figure S1 (Supporting Information) suggest the competitive coordination of the amine group to $Mg^{2+}$ in all the studied electrolytes, where the $NH_2$- peaks shifting to higher positions after adding salts to the solvents. It will be further studied in the following Nuclear Magnetic Resonance (NMR) analysis.

As shown in Figure 1c, the $^1H$ NMR spectra reveal the coordination behaviors of the solvent molecules. Compared to the pristine solvent, a noticeable peak shift is only observed from the $NH_2$ protons within the MPA-OTF electrolyte, which again verifies the monodentate solvent coordination to $Mg^{2+}$. Notably, chemical shifts were also observed from the protons that are adjacent to the ethereal group in both MEA-based electrolytes, suggesting the existence of some degree of bidentate coordination. The convergence of the spectroscopic results, informed by the DFT calculations to be discussed below, suggests the interpretations of the solvation structures of the three amine-based electrolytes which are presented as schematics in Figure 1d. The MEA-TFSI electrolyte contains fully dissociated anions and solvent-separated ion pairs (SSIPs), which can consist of a mixture of mono- and bidentate solvent coordination. The MEA-OTF electrolyte shows the coexistence of CIPs and SSIPs while the MPA-OTF electrolyte only has monodentate coordination with a significantly enriched CIP structure.

Pulsed-field gradient NMR (PFG-NMR) results shown in Figure 1e,f quantified the mass transport differences of the solvation species in the three electrolyte compositions. The MPA-OTF composition exhibits low solvent and anion diffusion coefficients compared to its MEA counterparts (and the neat solvent also diffuses more slowly than MEA), which is mainly attributed to the slightly higher viscosity (Figure 1g and Table S1, Supporting Information). More importantly, PFG-NMR was also used to evaluate the molecular weights of $^{19}F$ species in solution based on their Stokes radius, which aids in justifying the possible combinations of anion-involved solvation structures. The average molecular weights of anion-involved diffusion components are shown in Figure 1f. The value for the MEA-TFSI electrolyte (288.6 g $mol^{-1}$) is close to the molecular weight of free $TFSI^-$ anions (280.1 g $mol^{-1}$) and very consistent with the highly dissociated picture for this electrolyte, involving minimal cation–anion coordination. The MEA-OTF and MPA-OTF electrolytes, however, exhibit much higher molecular weights than the free $OTF^-$ (149.0 g $mol^{-1}$),

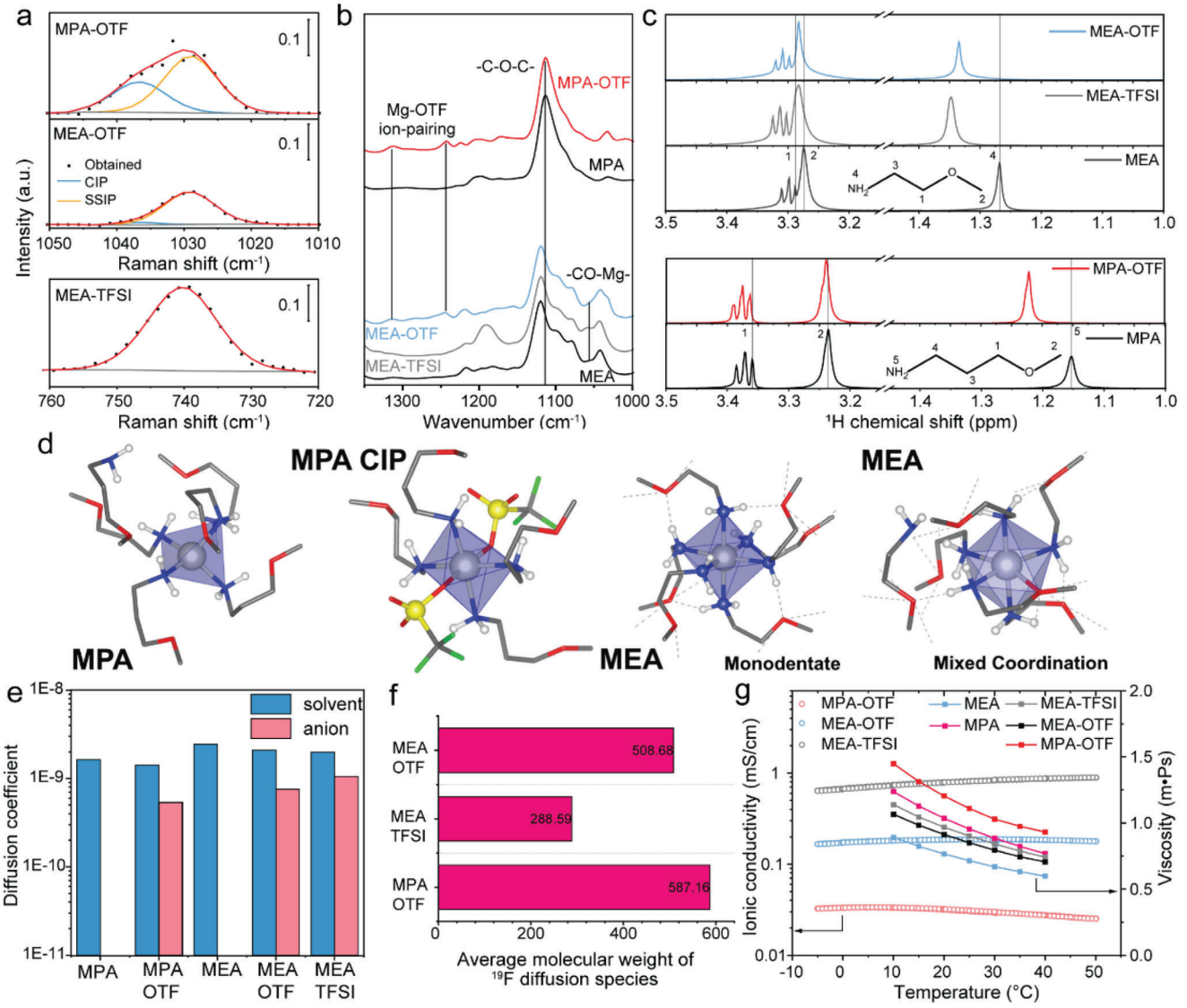


**Figure 1.** Analyzing $Mg^{2+}$ solvation and transport in amine electrolytes. The Raman spectra a) and FTIR spectra b) of the electrolytes with 0.1 M salts. c) The $^{1}H$ NMR spectra of the studied amine electrolytes and the comparison with the pristine solvents. d) The proposed schematic of possible solvation structures for the studied electrolytes. e) Solvent and anion diffusion coefficients from the studied electrolytes measured via PFG-NMR. f) The average molecular weights of $^{19}F$-containing species extracted from the diffusion measurements. g) The ionic conductivities and viscosities of the studied electrolytes and solvents at different temperatures.

implying that the $OTF^-$ anions have a significant residence time in ion aggregates. The extracted molar masses suggest average structures more consistent with $Mg(MPA)_4(OTF)_2$ and $Mg(MEA)_4(OTF)_2$. It is also important to note the direct correlations that exist between the solvation structures of the electrolytes and their physical properties, especially the ionic conductivity (Figure 1g and Figure S2, Supporting Information). The fully dissociated MEA-TFSI electrolyte shows the highest conductivity owing to its abundant free anions, while the electrolytes with CIPs have markedly decreased charge transport.[21] The MPA-OTF electrolyte, which corresponds to the combination of a weaker solvent and a strong-bonding salt, exhibits more than one order of magnitude reduction in conductivity relative to MEA-TFSI, again suggesting the existence of very strong anion participation in the solvation structures.[22,23] Such strong ion-pairing induced low conductivity from the OTF-based salt compared to the TFSI-based salt has also been confirmed in the lithium electrolytes.[23]

The range of ion-pairing degrees manifested by the electrolyte design choices was then tested through their electrochemical performance with a Mg metal anode. **Figure 2a** presents the cyclic voltammograms of the electrolytes with 0.1 M salt concentration in 3-electrode cells. The MEA-TFSI electrolyte demonstrates the highest reaction current density, with the complete order consisting of MEA-TFSI > MEA-OTF > MPA-OTF. However, the long-term CE tests of the electrolytes within standard Mg||stainless steel (SS) coin cells, shown in Figure 2b, exhibit a contradictory trend, wherein MEA-TFSI generated the lowest CE at ≈ 80.6%

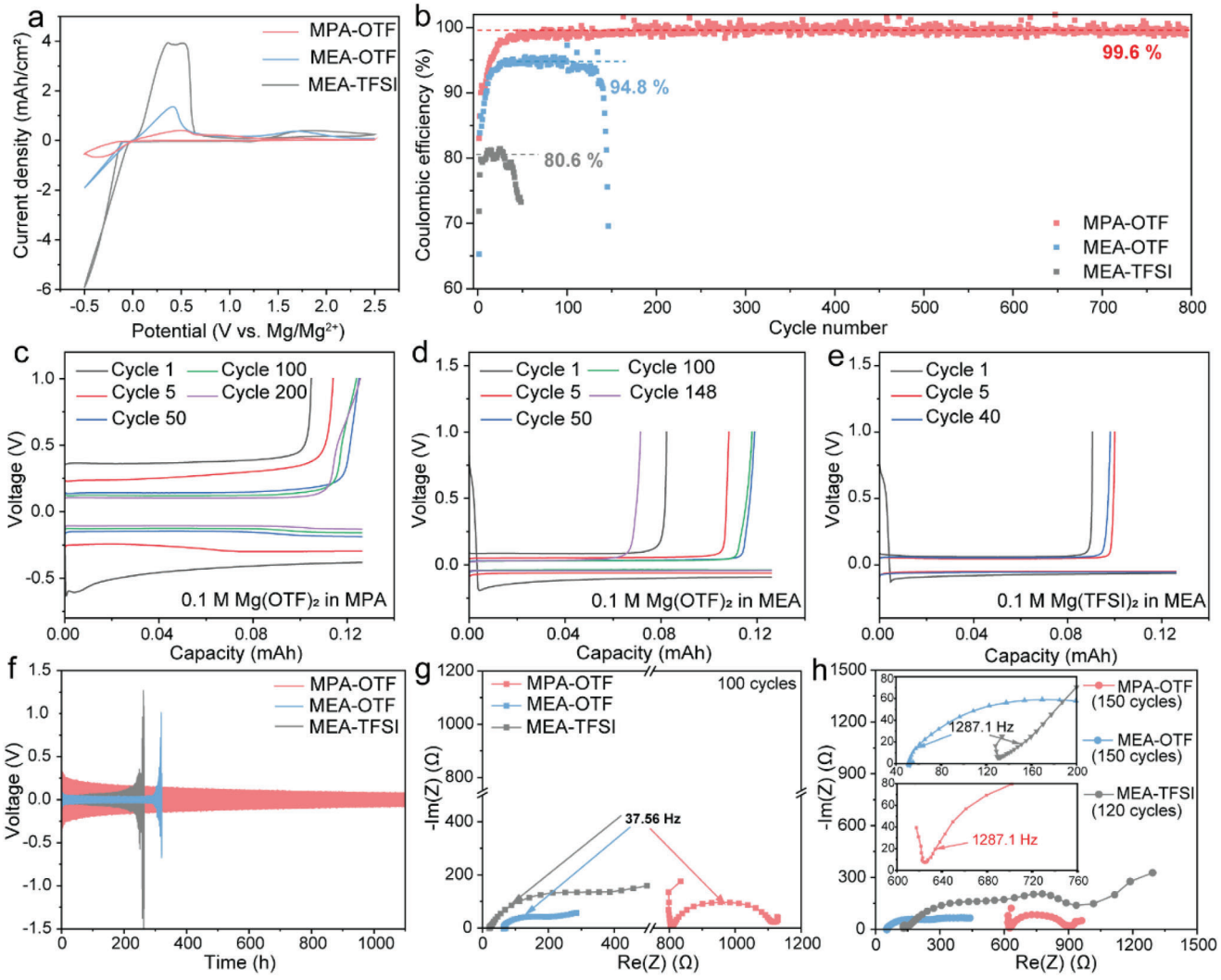


**Figure 2.** The electrochemical performance of Mg metal anode with the studied electrolytes. a. The cyclic voltammogram profiles between −0.5 to 2.5 V (vs. $Mg/Mg^{2+}$) of the electrolytes within 3-electrode cells where Mg metal serves as the counter and reference electrode, with Pt as the working electrode. b. The long-term cycling of the Mg||SS coin cells at a current density of 0.1 mA $cm^{-2}$ and capacity of 0.1 mAh $cm^{-2}$. c–e) The voltage-capacity profiles of the studied electrolytes at various cycle numbers. f) The long-term cycling voltage profiles of the symmetrical Mg||Mg coin cells at a current density of 0.1 mA $cm^{-2}$ and g) capacity of 0.1 mAh $cm^{-2}$. The EIS spectra of the symmetrical cells after 100 cycles and h) right before the cell failure for the MEA-OTF and MEA-TFSI electrolytes.

and resulted in a rapid battery failure (within 50 cycles). Simply changing the salt to $Mg(OTF)_2$ dramatically increased the average CE to 94.8% and extended the cycle life to 130 cycles. The ion-pairing MPA-OTF electrolyte in comparison, however, demonstrated impressive long-term stability over 800 cycles with an average CE of ≈ 99.6%. This, to the best of our knowledge, is by far the highest Mg metal plating–stripping CE ever reported without the introduction of any cosolvents or additives.[16,24] Figure 2c–e shows the voltage profiles of the Mg||SS cells, where the MEA-based electrolytes somewhat paradoxically produce smaller overpotential than the MPA-OTF electrolyte through the course of the testing, despite their much lower reversibility and cyclability.

Symmetrical Mg||Mg cell studies were therefore performed to characterize the interfacial behaviors of the electrolytes and interpret this intriguing performance. The long-term cycling results of the Mg||Mg cells in Figure 2f once again demonstrated the superior stability of the MPA-OTF electrolyte, which achieved >1000 h of cycling without any sign of battery failure. Similar stability at higher current densities was also realized in Figure S3 (Supporting Information). On the other hand, the MEA-based electrolytes cycled <350 h, with the MEA-TFSI electrolytes showing an even faster overpotential rise compared to the MEA-OTF.

Electrochemical impedance spectroscopy (EIS) performed periodically over the course of the symmetrical cell cycling revealed the different ion-conducting and charge-transfer behaviors. As shown in Figure 2g,h, the first intercept of spectra in the high-frequency range corresponds to the ion transport impedance in the bulk electrolyte.[25] This impedance for MPA-OTF is almost one order of magnitude higher compared to the MEA-based electrolytes and is therefore a primary contributor to its

larger overpotential during the cycling. In terms of the charge transfer impedance in the mid-frequency range (from ≈1000 to ≈1 Hz), which is generally considered to be the timescale of the rate-controlling step of Mg deposition–stripping,[8] the MPA-OTF electrolyte also does not confer any advantageous behavior (≈310 Ω vs. 131 Ω for the MEA-OTF and 128 Ω for the MEA-TFSI electrolyte). Therefore, the improved cycling stability of the MPA-OTF electrolyte must be attributable to some other factors apart from the interfacial charge transfer kinetics. Interestingly, we observed obvious cell swelling from the MEA electrolytes with both salts after the long cycling testing (Figure S4, Supporting Information). Simultaneously, as shown in Figure 2h and Figures S5 and S6 (Supporting Information), sudden ion-transport and charge-transfer limitations appeared in their symmetrical cell EIS profiles when cell failure was approaching. These observations indicate that a change in electrolyte composition or the interfacial environments at the Mg surface is taking place. On the other hand, these phenomena were never observed in the MPA-OTF cells. Gas evolution from the anode is generally associated with solvent reduction, and the direct $NH_2$ group reduction by alkali or alkali earth metals has also been reported with hydrogen release.[26,27] The gas that evolved from the MEA-TFSI electrolyte during cycling was analyzed via gas chromatography, as discussed in Figure S7 (Supporting Information). The hydrogen generation from the electrolyte reduction by the metallic Mg was confirmed. Therefore, we hypothesized that the presence of anion incorporation in the solvation structures can ameliorate the poor cathodic stability of the amine-based electrolytes and their extensive reaction with the Mg anode.

In order to probe the electrolyte decomposition during the cycling and the mechanism of rapid polarization buildup in the MEA-based electrolytes, we performed post-test characterizations of the Mg metal electrode and the electrolytes after cycling. As shown in Figure S8 (Supporting Information), X-ray photoelectron spectroscopy (XPS) was used to characterize the surface chemical compositions of the Mg metal anode after 5 formation cycles, as well as during the rapid overpotential growth. The primary detected components and their relative concentration are presented in **Figure** 3a–c, while the corresponding detailed fine spectra analyses are presented in Figure 3d. After cycling with MPA-OTF electrolyte, the C 1s spectrum shows a mains signal at 286.4 eV of polyether (C—O—C) and small signal from carbonyl (C═O)-containing species. The broad signal of N 1s spectrum consists of C—N, C—$NH_2$, and N—O containing species. The Mg 2p spectrum confirms the presence of Mg metal together with MgO and $MgCO_3$. These signals originated from the decomposition of MPA as the only source of nitrogen and ether functional group from the electrolyte. In addition, the decomposition of anion ($OTF^-$) is evidenced by the presence of fluoride and sulfide species but at low concentration (< 2 at. %) (Figure S9, Supporting Information). This result suggests that the SEI formed in MPA-OTF is mainly contributed by MPA solvent decomposition. The Mg anode in the MPA-OTF electrolyte demonstrated consistent SEI compositions after thorough cycling, where minimal concentration evolution was observed for all the components. These results correspond well with its high CE, suggesting a negligible electrolyte decomposition occurred during cycling. In comparison, the Mg electrode cycled in MEA-OTF electrolyte shows a similar composition of SEI layer to that formed in MPA-OTF electrolyte in early cycles. The unique nitrite ($NO_2^-$) species at ≈ 404.8 eV stemming from the MEA-based electrolytes is a signature of MEA decomposition.[28] However, the enrichment of —C═O signal in C 1s and $MgCO_3$ signal in Mg 2p with increased cycle number suggests a continuous solvent decomposition occurred at the interface.[29] This was supported by the decreased concentration of metallic Mg in Mg 2p due to the thickening of the passivation layer. The solvent decomposition is more severe in the MEA-TFSI electrolyte, where the Mg-associated compounds (mainly comprised of MgO, $MgCO_3$, and $Mg(OH)_2$) are enriched to ≈ 40 at. % of the total Mg content (with decreasing Mg metal signal) upon cycling. The inorganic fluorinated product $MgSO_xF_y$ was only detected in the SEI from this electrolyte, demonstrating that it also promotes TFSI anion decomposition. A higher concentration of sulfide (Figure S9, Supporting Information) was also observed in Mg electrode cycled in MEA-TFSI electrolyte compared to its OTF-based counterpart. This implies that the decomposition of TFSI also contributed to the passivation of Mg anode, leading to poor electrochemical performance of $TFSI^-$based electrolyte.

The surface morphologies of the Mg deposition for the different electrolytes were analyzed by scanning electron microscopy (SEM) with energy-dispersive X-ray (EDX) spectroscopy. From Figure 3e–g, the MPA-OTF electrolyte resulted in uniform and dense deposition with the least porosity. Such behavior is beneficial in reducing parasitic side reactions. The MEA-OTF electrolyte induced noticeable porosity into the plated Mg, where both large granular morphology and smaller particles can be observed. In sharp contrast, the Mg deposition with the MEA-TFSI electrolyte appeared as the aggregation of tiny particles that were sized between 500 nm and 5 µm. The entire electrode is highly pulverized, with inhomogeneous distributions on the substrate. The deteriorated morphology corroborates the consistency between the inferior electrochemical cycling stability and the observed reactivity of the liquid electrolyte toward Mg metal. The EDX mapping of the plated Mg metal (Figure S10, Supporting Information) suggests that these mainly contained Mg, O, and C species, while F species comprise < 1%, again consistent with the prior observations of solvent decomposition dominating the SEI formation.

Overall, the analyses of SEI composition evolution and Mg deposition behaviors are consistent with the electrochemical results. The MPA-OTF electrolyte shows higher reduction stability and prohibits the continuous solvent decomposition at the interface leading to the SEI accumulation. Alleviating the solvent reduction and $H_2$ evolution not only increases the interfacial stability but also promotes more uniform Mg plating. However, the precise mechanism for how the solvation structures affect the electrolyte interfacial stability is as of yet unclear, especially with regard to why the OTF-involved CIPs possess higher stability. More importantly, the change in SEI compositions for the MEA-based electrolyte in Figure 3a–d seems insufficient to cause complete battery failure, as most of the concentrations changed by < 5%. The SEI evolution cannot therefore be considered as dramatic based on the EIS and XPS results, even when the batteries approached failure. Accordingly, it is reasonable to speculate that the solvent decomposition products are soluble in the electrolytes, as opposed to precipitating in the SEI.

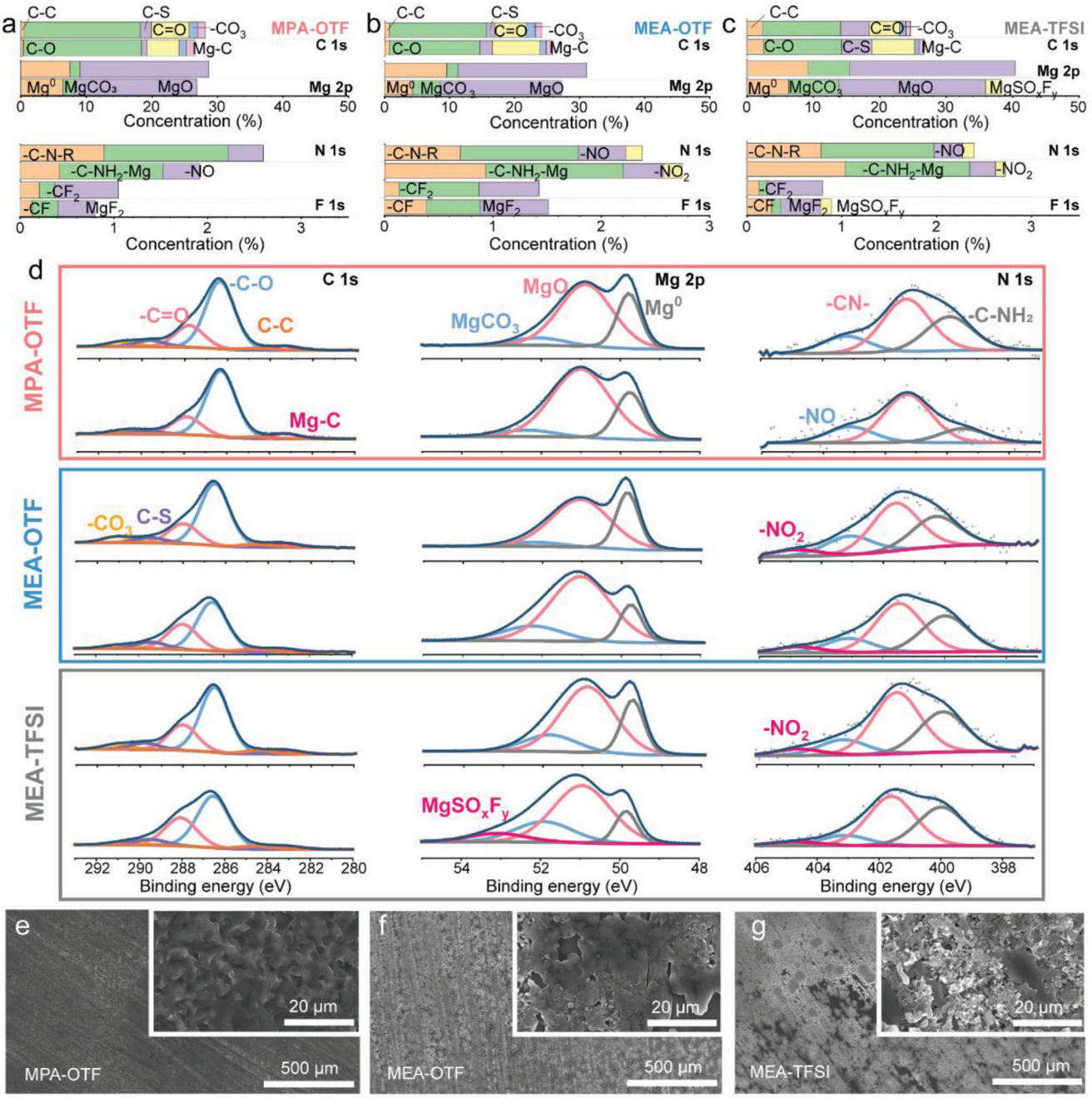


**Figure 3.** Investigating the SEI formation on the Mg metal anodes and their plating morphology. a–c) The relative concentrations of the detected C 1s, Mg 2p, and F 1s species on the Mg metal anodes from different electrolytes. The upper and lower column from each element refers to the anode after five cycles and long-term cycling, respectively. d) The corresponding fine spectra analyses. e,f) The top view of the surficial morphology of plated Mg onto the Mg metal substrate. The areal capacity is 0.4 mA $cm^{-2}$.

To identify the possible decomposition products that are soluble and escaped detection by XPS, we used ex situ $^{1}H$, $^{13}C$, and $^{19}F$ NMR to analyze the deeply cycled electrolytes within the symmetrical Mg||Mg cell. As demonstrated by the digital pictures of the beaker-type symmetrical cells in Figure S11 (Supporting Information), the MEA-TFSI electrolyte continuously bubbles during the galvanostatic cycling due to solvent dehydrogenation. The gas generation was self-sustained even after cutting off the current, which suggests this electrolyte can spontaneously react with fresh Mg metal. While no obvious gas release can be observed from the MEA-OTF cell. The cycled electrolytes were then subjected to the following NMR studies. **Figure** 4a shows the results from the cycled MEA-TFSI electrolyte, where obvious side reaction components can be observed from all three spectra. Considering that the intensities of the new $^{13}C$ peaks are very comparable to those of the $TFSI^{-}$ anion (located at ≈ 120 ppm), the

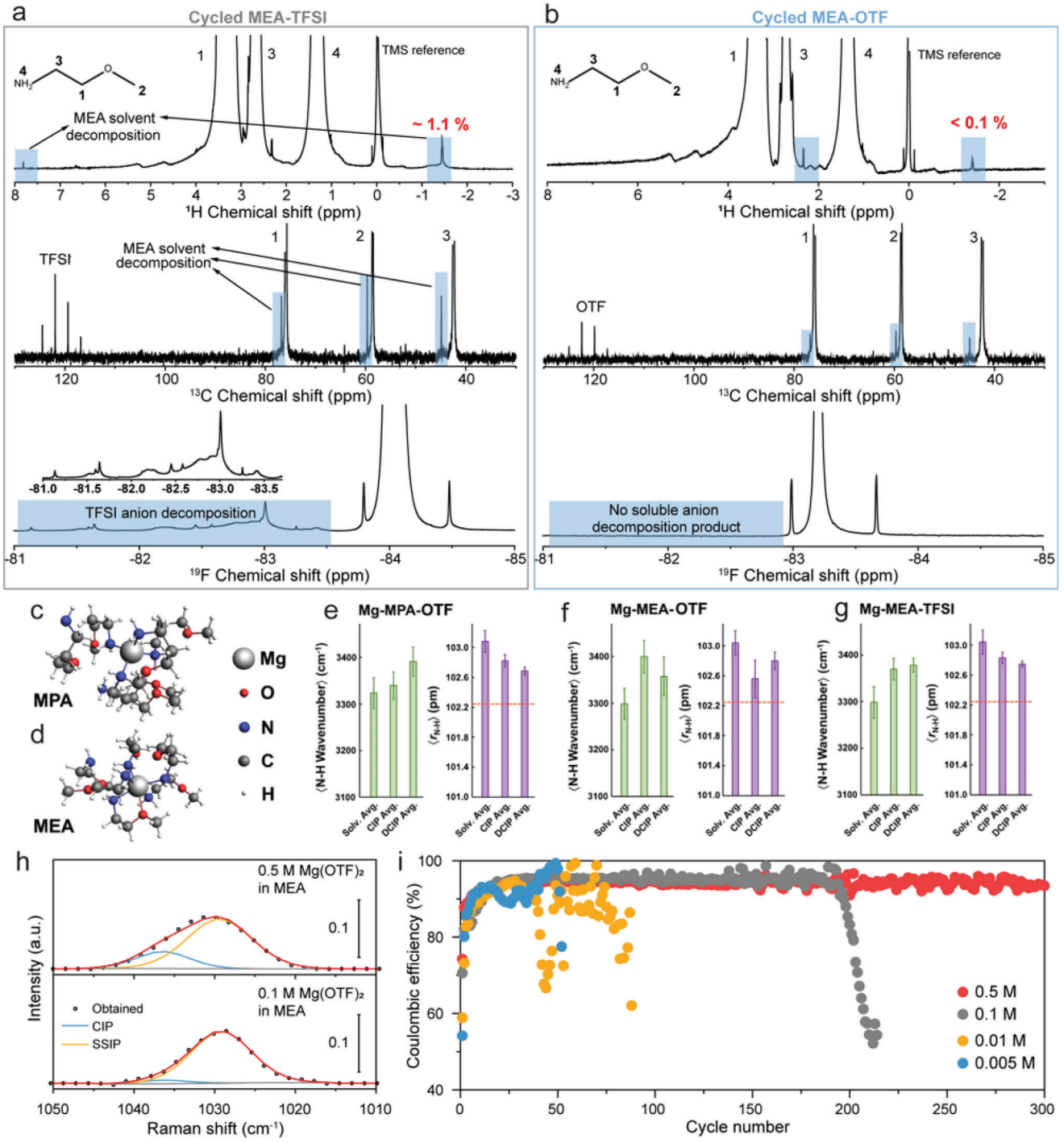


**Figure 4.** The reduction reactivities of the most probable solvation species in the amine-based electrolytes. The $^{1}$H, $^{13}$C, and $^{19}$F spectra of deep-cycled a) MEA-TFSI and b) MEA-OTF, illustrate the composition and relative amounts of the soluble solvent and anion decomposition products. The DFT-calculated, lowest-energy solvation structures for $Mg^{2+}$ in MPA c) and MEA d), respectively. The PVDOS weighted-average wavenumber and average N—H bond length for the Mg-coordinated amine groups (separately averaged over the purely solvated, CIP, and DCIP cluster classes) for the e) MPA-OTF, f) MEA-OTF, and g) MEA-TFSI systems, serving as metrics for the N—H bond strength with and without anion incorporation in the solvation shell (the dashed line gives the computed N—H bond length in neat MPA, with the uncertainty contained in the width of the line). h) The prevalence of CIP species in pristine MEA-OTF is confirmed with Raman spectra of the 0.1 M and 0.5 M electrolyte mixtures, i) with the pronounced effect of CIP stabilization of the solvation on cycling behavior demonstrated in.

irreversible reduction of MEA solvent is very intensive, with the side reaction product concentration reaching up to the hundred-mM level. The results also demonstrate our hypothesis that the major parasitic reactions from the MEA-TFSI system originate from solvent decomposition, whose products are not preserved in the SEI but instead diffuse into the electrolyte.

Moreover, the most significant new $^{1}H$ peak in Figure 4a possesses a highly irregular negative chemical shift when compared with the pristine electrolyte (Figure S12, Supporting Information), which correlates to an enrichment of electron density to that H atom in the newly generated species. The new $^{13}C$ peaks with similar intensities are found consistently at higher frequencies relative to the original peaks. Their corresponding shift deviations from the original (i.e., adjacent), pristine electrolyte peak positions are of magnitude $\Delta C_3 > \Delta C_1 > \Delta C_2$, an order which is consistent with their corresponding intramolecular distances to the nitrogen atom. Therefore, it is reasonable to speculate that the reduction of MEA molecule does not break the alkyl chain of the solvent molecule, only creating a strong electron-withdrawing center at the N atom. Combining this observation with the observed $H_2$ gas evolution, we propose the following reaction for the MEA decomposition at the anode:

$$\frac{x}{2}Mg^{0} + [Mg^{II}(H_2NCH_2CH_2OCH_3)_x] \rightarrow \frac{x}{2}Mg^{II}(HNCH_2CH_2OCH_3)_2 + Mg^{2+} + \frac{x}{2}H_2 \quad (1)$$

$$\left[Mg^{2+}\left(H_2NCH_2CH_2OCH_3\right)_x\right] + xe^{-} \rightarrow \frac{x}{2}Mg^{II}\left(HNCH_2CH_2OCH_3\right)_2 + \left(1-\frac{x}{2}\right)Mg^{2+} + \frac{x}{2}H_2 \quad (2)$$

where Equation 1 stands for the spontaneous reduction of the coordinated MEA by the Mg metal, and Equation 2 stands for the electrochemical reduction. There is a direct interaction between the Mg and the H from the amine group with the possible structure of Mg—HN—R.[30] Considering the MEA-TFSI electrolyte can react with Mg metal spontaneously or electrochemically, the cell failure is dependent on both cycling numbers and time. Note, however, that the $^{19}F$ spectrum after the deep cycling also indicates the presence of some soluble anion reduction products. Therefore, the low reversibility of MEA-TFSI electrolytes is attributed to the parasitic reduction reactions that originate from both MEA solvent and the free $TFSI^{-}$ anions. Therefore, we believe the failure of the cell should be dependent on both time and cycling numbers so as to provide fresh Mg metal and reaction time to consume the liquid electrolyte. To validate the electrolyte consumption mechanism, especially the product dissolution behavior, an electrolyte replenishment test was performed with the MEA-TFSI electrolyte, as shown in Figure S13 (Supporting Information). The symmetrical Mg cell after failure was opened and replenished with fresh liquid electrolyte. Normal cell cycling with similar overpotential can be resumed after adding the fresh electrolyte. It indicates that the MEA-TFSI electrolyte reduction generates products that can easily dissolve into the electrolyte, instead of completely accumulating in the SEI.

In sharp contrast, changing the salt from $Mg(TFSI)_2$ to $Mg(OTF)_2$ largely suppressed the electrolyte decomposition. As shown in Figure 4b, similar solvent decomposition products were captured from the cycled MEA-OTF electrolyte compared to the MEA-TFSI, but to an extent of one magnitude lower (< 0.1% vs ≈ 1.1%). This indicates that there exist similar solvent decomposition pathways within both MEA-based electrolytes but with significantly reduced reaction rates for the MEA-OTF electrolyte. The clean $^{19}F$ spectrum after cycling demonstrates minimal $OTF^{-}$ anion decomposition in this case, as would be expected given the higher intrinsic stability against reduction of $OTF^{-}$ compared with $TFSI^{-}$. It has been reported in previous works that the OTF anion is intrinsically more stable than the TFSI anion toward reduction.[31] The lowest unoccupied molecular orbital (LUMO) energy level of the $TFSI^{-}$ facilitates its reduction on the anode surface. Here, the results indicate that $TFSI^{-}$ reduction from the MEA-TFSI electrolyte not only generates inorganic compounds that accumulate in the SEI but also produces soluble small fluorinated molecules. On the contrary, OTF-based electrolytes are less prone to anion decomposition, which mitigates the overall parasitic reactions and improves the anode efficiency. It is also verified by the XPS results that the MEA-TFSI electrolyte induced more complete anion decomposition.

Now if revisiting the long-term CE studies in Figure 2b, it took many cycles (≈ 50) for MPA-OTF to reach the stabilized efficiency due to the low current density and areal capacity applied. It is the traditional "conditioning process" that suggests the passivation behavior of the SEI. Its solvent reduction products are insoluble and accumulate in the SEI to prohibit further decomposition once formed. On the contrary, although the MEA-based strong-coordinating electrolytes generate SEI with similar components as the MPA electrolyte, they are, in the meantime, subject to the dehydrogenation reaction whose products are highly soluble in the liquid electrolyte. Such dehydrogenation reaction is thus unable to be kinetically suppressed by the formed SEI, so it renders consistently low efficiency.

In order to confirm the elucidated solvation structures and the trends associated with ion pairing and stability of the electrolyte blend against electrochemical reduction, DFT calculations were performed on a series of clusters generated based on the permutations that the solvation could, in principle, encompass (e.g., fully solvated vs. CIP vs. double CIP (DCIP); mono- vs bidendate solvent and anion coordination; coordination symmetry ranging from threefold to octahedral; refer to Table S2 (Supporting Information) for a complete index). These idealized cluster configurations were then geometry-optimized, and their vibrational spectra and approximate Gibbs energies of formation were computed to facilitate relative comparison (refer to the DFT methods section, vide infra). The optimized structures for the MPA-OTF, MEA-OTF, and MEA-TFSI systems are presented in Figures S14–S18 (Supporting Information), which in some cases deviated significantly from the originally intended coordination/pairing degree; all subsequent analysis is nevertheless conducted on the output from the geometry optimization since there is a high degree of polymorphism evidenced for the solvated configurations (see Figure S19, Supporting Information). Optimized coordinates for all configurations tested are supplied in the Supplementary attachment. Nevertheless, the calculations indicate that the MPA-OTF system has a clear preference for fourfold-coordinated solvation. The lowest-energy solvation configurations for MEA-OTF and MPA-OTF are given in Figure 4c,d. In all three studied electrolytes, N-coordination is preferred to

O-coordination for monodentate configurations, consistent with the spectroscopic results in Figure 1. The energy gap between solvated and ion-pairing clusters with the $OTF^-$ anions is significantly smaller than for $TFSI^-$, again consistent with the relatively small degree of CIP formation evidenced in Figure 1 for MEA-TFSI, contrasted with a virtual continuum of formation energies for MEA-OTF and a practical degeneracy between all tested CIP and DCIP configurations for MPA-OTF. There is little influence of temperature in the relevant range (273–323 K) on the relative energetics of the solvated versus ion-pairing clusters in all cases.

To assess the influence of anion incorporation on the stability of the cluster configurations against $H_2$ evolution, the strength of the N—H bond in Mg-coordinated amine groups was assessed using two metrics derived from the computational results: the weighted-average wavenumber of the N—H partial vibrational density of states (PVDOS) for modes involving only the N—H bonds in Mg-coordinated amine groups (designated ⟨N-H Wavenumber⟩ in Figure 4e–g), and the average calculated length of such bonds in the optimized structures (written $\langle r_{N-H} \rangle$ in Figure 4e–g). The computed overall IR spectra are provided in Figures S20–S22 (Supporting Information) for completeness, with the N—H PVDOS decompositions for comparison presented in Figure S23 (Supporting Information). Integrating the PVDOS in the region of interest yields a simple and unified means of comparison across the different permutations of coordination and anion incorporation (values for the specific configurations leading to the averages in Figure 4e–g are plotted in Figure S24, Supporting Information). For all three electrolytes, the average N—H wavenumber is shifted to lower values with purely solvated configurations relative to CIP and DCIP configurations, indicating that the inductive effect of the anion incorporation strengthens the N—H bonds of the Mg-coordinating amines and thereby boosts their stability against reduction, though the comparative paucity of CIPs in solution for MEA-TFSI, in particular, mitigates this benefit in its case. The increased N—H bond strength of the CIP and DCIP configurations is also directly evident in the correspondingly reduced bond lengths (values leading to the averages over the distinct cluster classes are plotted in Figure S25, Supporting Information), with the increased bonding strength commensurately attenuating the N—H bond breaking likely accompanying $H_2$ generation. However, a more detailed study of the reaction mechanism and computation verification of Equation 1 is needed to elucidate the interfacial gas evolution process in amine based solvents.

The concordant results of the range of techniques presented in this study justify the correlations between the solvation environments of the electrolytes and the cathodic stability of amine solvent molecules. As demonstrated by contrasting the MEA-TFSI < MEA-OTF < MPA-OTF cycling performance and the relative amounts and types of decomposition products produced by each, it is clear that introducing the $OTF^-$ anion to the primary solvation shell can largely suppress the direct reduction of the $NH_2$ group by Mg metal. Lastly, we tested the cycling stability of the MEA electrolytes with increasing $Mg(OTF)_2$ concentrations, with results shown in Figure 4h,i. The Raman spectra of 0.1 and 0.5 M $Mg(OTF)_2$ in MEA exhibited the expected enhancement in the relative concentration of CIPs. The CE testing of the electrolytes with salt concentrations of 0.005, 0.01, 0.1, and 0.5 M again confirms the direct influence of CIP concentrations on the Mg anode cycling stability, where the 0.1 M electrolyte failed within 200 cycles while the 0.5 M electrolyte cycle life extended beyond 300 cycles. The high concentration (0.5 M, near saturation) of MEA-OTF didn't outperform the MPA-OTF electrolyte (0.1 M, near saturation) in terms of anode efficiency. The results suggest that using an intrinsically weaker solvent is more effective than improving the salt concentration to soften the coordination to cation. The MEA molecule is still subjected to reduction due to its strong coordination nature.

It's important to note that the ion-pairing strategy via introducing strongly coordinating anions into the solvation shell to weaken the solvent coordination can improve its stability and prohibit decomposition. However, this strategy inevitably reduces the ion transport kinetic due to the low salt dissociation degree and ionic conductivity. The low-concentration amine electrolytes containing abundant free $-NH_2$ groups are also susceptible to oxidation. Therefore, the MPA-OTF electrolyte can only be considered as a proof-of-concept that rationally alleviates the amine reduction, instead of a mature Mg electrolyte that can enable direct practical applications. For future works, we believe it's critical to improve the overall concentration of the CIPs to undertake the $Mg^{2+}$ transport. Introducing a second salt into the electrolyte is expected to increase the $Mg(OTF)_2$ solubility and improve the overall concentration. For example, adding $Mg(TFSI)_2$ salt into the MPA-OTF electrolyte to form a binary salt electrolyte can improve the OTF solubility. Investigating salt chemistry is another possible pathway to find an optimized anion with balanced coordinating strength and dissociation capability.

## 3. Conclusion

In this work, we studied a set of amine-based RMB electrolytes with a series of compositions engineered to yield a spectrum of ion-pairing strength and examined their interfacial reduction stabilities and decomposition behaviors on a Mg metal anode. It was demonstrated that structures with strong cation-solvent coordination have low reduction stabilities against an Mg anode, particularly with regard to the $NH_2$ group. $H_2$ evolution from amine group reduction was identified as the main parasitic reaction. Introducing an anion into the solvation structure by employing a less-coordinating solvent and a comparatively weakly dissociating salt can effectively strengthen the N—H bond in the amine group by reducing its interaction with the $Mg^{2+}$ cation. Correspondingly, the weakly coordinating amine solvent MPA, which generates copious CIP structures in the electrolyte, demonstrated outstanding stability and reversibility of Mg deposition. It achieved a 99.6% CE in long-term cycling, with over 800 cycles completed. A unique dissolution behavior of the solvent decomposition product was demonstrated which compromises the interfacial stabilization in the strongly coordinated amine-based electrolytes. The dehydrogenation reaction products from the electrolyte reduction solubilize and tend to diffuse into the electrolyte instead of accumulating in the SEI, which fails to passivate the Mg surface, causing continuous electrolyte consumption. Therefore, this work both generates new insights into the interfacial behaviors of Mg electrolytes and proposes an effective strategy to design nonaqueous electrolytes for secondary Mg batteries.

## 4. Experimental Section

*Materials*: The 2-methoxyethylamine (MEA) (99%) and 3-methoxypropylamine (MPA) (99%) were purchased from Sigma-Aldrich. They were dried with activated 3Å molecular sieves for one week before use. The magnesium trifluoromethanesulfonate ($Mg(OTF)_2$) (99.5%) and magnesium bis(trifluoromethanesulfonyl)imide ($Mg(TFSI)_2$) (99.5%) were purchased from SOLVIONIC and used without any further treatment. Mg metal single crystal foil with a thickness of 100 µm was obtained from MTI Corp.

*Electrochemical Tests*: Each studied electrolyte was prepared by dissolving 0.1 mmol of salt into 1 mL of amine solvent. They were stirred until the salts were completely dissolved. The Mg foil was thoroughly scraped by a stainless-steel razor blade to remove its surface passivation layer and cut into disks (Ø 12.7 mm) before use. Whatman glass fiber paper was used as the separator in the cells. It was dried at 120 °C in the vacuum oven and immediately transferred to the glovebox. All the cell preparations were carried out in an Ar-filled glove box with $O_2$ and $H_2O$ concentrations < 0.3 ppm. The CV tests were performed within 3-electrode Swagelok cells, where Mg disks were used as reference and counter electrodes, while the same size of Pt disk served as the working electrode. 200 µL electrolyte was added to the cells. They were scanned between −0.5 to 2.5 V (vs. $Mg/Mg^{2+}$) under a 10 mV $s^{-1}$ scan rate.

Other electrochemical tests were carried out in 2032 coin-type cells. The Coulombic efficiency was tested with Mg||SS cells. The stainless-steel substrates were carefully polished by alumina powder (≈1 µm) until mirror-shining and then used for deposition. The Mg||SS cells were assembled with the Mg metal disk, glass fiber separator, and 150 µL electrolyte. The CE was determined by calculating the ratio of stripping capacity over the deposition capacity throughout the long-term cycling. The Mg||Mg symmetrical cells were assembled in the same way as Mg||SS cells except using Mg disks for both electrodes and the cathode lid polishing was not necessary.

*Materials Characterization*: The densities and viscosities of the amine-based electrolytes were measured by the Anton Paar DMA 4500 M platform with a Lovis 2000 ME rolling-ball viscometer. The data were collected between 10 °C and 50 °C with an increment of 5 °C. The ionic conductivities of the electrolytes were measured by an MCS-10 conductometer from Biologic Science Instruments between −5 °C and 40 °C.

The FTIR spectra of the electrolytes were collected with a Bruker Alpha II instrument under an Ar atmosphere at 25 °C in the glovebox. The samples were scanned from 4000 to 400 $cm^{-1}$ with a spectral resolution of 2 $cm^{-1}$. The samples for Raman spectroscopy of electrolyte solutions were prepared by filling the as-prepared solution in a sealed glass NMR tube (5 mm, Wilmad NMR tubes, Sigma Aldrich) under an Ar atmosphere. Raman spectroscopy measurement was performed using an in-house spectrometer equipped with a 633 nm laser and a CCD detection system (Andor, Shamrock 303i, and iDus 416). The objective lens of the Raman microscope was placed on the curved edge of the NMR tube with the laser beam intensity of 2–3 mW focused on the sample surface. The Raman data shown is spatially (10 spectra in a 1 × 1 $mm^2$ area) and temporally (integration time of 360 sec per spectra) averaged to ensure sample integrity throughout the measurements. The Raman spectra were deconvoluted using Casa XPS. A Shirley-type baseline was used for all the spectra.

$^1H$, $^{19}F$, and $^{13}C$ NMR spectra were obtained at 25 °C in a 500 MHz NMR spectrometer (Agilent, USA) with a 5-mm HX probe at the Larmor frequencies of $2\pi \times 499.901$, $2\pi \times 470.412$, and $2\pi \times 125.714$ rad·MHz, respectively, by using single pulse excitation. The chemical shift of 0 ppm for the $^1H$ and $^{13}C$ NMR spectra were calibrated with tetramethylsilane (TMS), which was added to the solutions. The $^{19}F$ chemical shift was calibrated with 2-2-2-trifluoroethanol ($CF_3CH_2OH$) of78 ppm as an external reference. Thank for the comment. The 1H NMR peaks were assigned using the software provided on the website: https://www.nmrdb.org/new_predictor/index.shtml?v = v2.138.0. This software was developed based on 1) Banfi, D.; Patiny, L. www.nmrdb.org: Resurrecting and processing NMR spectra on-line Chimia, 2008, 62(4), 280–281,[32] 2) Andrés M. Castillo, Luc Patiny and Julien Wist. Fast and Accurate Algorithm for the Simulation of NMR spectra of Large Spin Systems. Journal of Magnetic Resonance 2011,[33] and 3) Aires-de-Sousa, M. Hemmer, J. Gasteiger, "Prediction of 1H NMR Chemical Shifts Using Neural Networks", Analytical Chemistry, 2002, 74(1), 80–90.[34]

The surface morphology of Mg deposition was observed by an environmental scanning electron microscope (ESEM, Quanta 3d FEG, Thermo Fisher Scientific) coupled with an energy-dispersive X-ray spectroscopy (EDX, Oxford Instruments) to probe the spatial distribution of C, O, and Mg. The Quanta ESEM was equipped with an FEI Quanta digital field emission gun. The ESEM was operated at 20 kV electron accelerating voltage and 480 pA current under vacuum conditions (1.2 × 10–6 torr pressure). The samples were prepared in the Mg||Mg coin cells where an extra piece of polypropylene separator (Celgard 2500) was placed between the glass fiber and Mg metal electrode. The cells were cycled five times at 0.2 mA $cm^{-2}$ for a period of 2 h, followed by a 2 h Mg deposition with the same current density to one side of the symmetrical cell. The cells were disassembled in the glovebox and the Mg-deposited electrodes were harvested from the cells and rinsed by their corresponding electrolyte solvents. They were then dried under vacuum at room temperature and loaded onto the SEM sample holders for observation.

The XPS samples were prepared in the same way as the SEM samples except that different numbers of pre-cycling steps were performed before the last deposition step. The cells were opened in the Ar-filled glovebox with moisture and oxygen < 1 ppm. After rinsing the electrodes with the electrolyte solvents, they were quickly loaded onto the sample holder and transferred into the XPS high vacuum chamber to minimize the possible side reactions and/or contamination. The samples were then transferred to XPS analysis chamber using in vacuo transfer mechanism without being exposed to air and contamination sources. The XPS spectra were collected using a Kratos Axis Ultra DLD spectrometer, which consists of an Al K$\alpha$ monochromatic X-ray source (1486.6 eV) and a high-resolution spherical mirror analyzer. The X-ray source was operated at 150 W power and the emitted photoelectrons were collected at the analyzer entrance slit normal to the sample surface. The high-resolution spectra were collected at a pass energy of 40 eV with a step size of 0.1 eV. The XPS measurement was conducted without applying a charge neutralizer. The CasaXPS software was used to analyze the data. All the XPS peaks were charge referenced to Mg 2p signal of metallic Mg at 49.7 eV.

*DFT Methods*: DFT calculations were performed using the Amsterdam Density Functional (ADF) engine of the Amsterdam Modelling Suite, v2022.1 (SCM, Theoretical Chemistry, Vrije Universiteit, Amsterdam). Clusters of solvents and/or anions coordinating the central divalent cation were constructed, with permutations of coordination number, mono- versus bi-dentate coordination, and stereochemical arrangement considered for each cluster (refer to Table S2, Supporting Information for a complete index). These initial clusters were sequentially pre-optimized using universal force field (UFF) molecular mechanics[35] and density functional-based tight binding (DFTB) methods.[36] Geometry optimizations were then carried out using the Becke-Lee-Yang-Parr (BLYP) exchange-correlation functional,[37,38] at the augmented triple-zeta, single polarization (AZTP) basis set level (all-electron) and using scalar relativity and D3 dispersion corrections.[39] In order to balance the tradeoff between the computational expense of the normal modes calculation and the accuracy necessary for reasonable spectroscopic predictions, a "Good" numerical quality setting was employed, corresponding to a convergence criterion of <0.004 mHartree energy difference between iterations (refer to Franchini et al., 2013[40] for more details on the convergence criteria). The basis set dependency check in ADF was active for the geometry optimizations.

The optimized geometries were used to compute normal modes of vibration (with mode rescanning active to remove spurious imaginary modes), which were used to generate simulated IR spectra (FWHM: 15 $cm^{-1}$). The normal modes were then also used to calculate the Gibbs free energy differences between the optimized cluster configurations, using the harmonic oscillator/free rotor interpolation scheme for the correction of low energy modes (< 20 $cm^{-1}$),[41,42] via the following approximate (gas-phase) reaction scheme:

$$MgA_2 + 6S \rightleftharpoons [MgS_{6-n}A_n]^{(2-n)+} + (2-n)\,A^- + nS \quad (3)$$

$$\Delta G_{corr} = G\left([MgS_{6-n}A_n]^{(2-n)+}\right) + (2-n)\,G(A^-) - \Delta G_{ion} - G(6S) \quad (4)$$

$$\Delta G_{ion} = \begin{cases} IE_1(Mg) + IE_2(Mg) - 2EA(A), & n = 0 \\ IE_1(Mg) - EA(A), & n = 1 \\ 0, & n = 2 \end{cases} \quad (5)$$

where $A = \{TFSI, OTF\}$, $S = \{MEA, MPA\}$, $\Delta G_{rxn}$ is the Gibbs energy change of the cluster formation, $\Delta G_{ion}$ is the net Gibbs energy change of the $MgA_2$ salt ionizing, $IE_x$ is the $x^{th}$ ionization energy, EA is electron affinity, and $n$ is the index for degree of contact ion pairing. Here, the cationic ionization energies and the salt electron affinities were used as an approximation for the unavailable Gibbs energy change of ionization for both $Mg(TFSI)_2$ and $Mg(OTF)_2$, in order to facilitate comparison between clusters with different overall charges. $Mg^{2+}$ ionization energies were obtained from NIST,[43] and electron affinities for $TFSI^-$[44] and $OTF^-$[45] were sourced from the literature. The weighted-average wavenumber of the Mg-coordinated N—H PVDOS as a simple bond strength metric readily comparable between different cluster configurations was computed by selecting the subset of modes that only involved N—H motions, exclusively for N—H coordinated to Mg, and numerically integrating the resulting partial spectrum. All error bars in computed properties averaged over the cluster ensembles were standard errors of the mean calculated via the variance formula.

## Supporting Information

Supporting Information is available from the Wiley Online Library or from the author.

## Acknowledgements

This work was supported by the Joint Center for Energy Storage Research (JCESR), an Energy Innovation Hub funded by the U.S. Department of Energy, Office of Science, Basic Energy Sciences (BES). A portion of NMR research was performed using EMSL (grid.436923.9), a DOE Office of Science User Facility sponsored by the Office of Biological and Environmental Research. PNNL is a multiprogram national laboratory operated for the DOE by Battelle Memorial Institute under Contract DE-AC06-76RLO 1830.

## Conflict of Interest

The authors declare that they have no conflict of interest.

## Author Contributions

Z.L. and D.-T.N. contributed equally to this work. Z.L. conceived the idea. V.M. supervised the project. Z.L. designed the experiments with D.T.N. and V.M. Z.L. performed electrolyte preparation, characterizations, and electrochemical tests. J.D.B. and V.M. performed the DFT calculations and J.D.B. wrote the computational section. D.T.N. collected the XPS spectra, and Z.L. analyzed the results. K.S.H and Y.C. performed the NMR study. V.P. collected the Raman spectra. T.T.L carried out the hydrogen detection experiment. Z.C. analyzed the samples with SEM. M.S. tested the electrolyte conductivity. K.T.M. V.G.P. and V.M. provided important insights during the project design and supervision. Z.L. wrote the paper with contributions from all authors.

## Data Availability Statement

The data that support the findings of this study are available from the corresponding author upon reasonable request.

## Keywords

amine solvents, Mg Anode, multivalent batteries, non-aqueous electrolytes

Received: May 21, 2023
Revised: February 1, 2024
Published online: March 8, 2024

[1] R. Deivanayagam, B. J. Ingram, R. Shahbazian-Yassar, *Energy Storage Mater.* **2019**, *21*, 136.
[2] R. Mohtadi, O. Tutusaus, T. S. Arthur, Z. Zhao-Karger, M. Fichtner, *Joule* **2021**, *5*, 581.
[3] Y. Liang, H. Dong, D. Aurbach, Y. Yao, *Nat. Energy* **2020**, *5*, 646.
[4] I. Shterenberg, M. Salama, H. D. Yoo, Y. Gofer, J. B. Park, Y. K. Sun, D. Aurbach, *J. Electrochem. Soc.* **2015**, *162*, A7118.
[5] Y. Shao, T. Liu, G. Li, M. Gu, Z. Nie, M. Engelhard, J. Xiao, D. Lv, C. Wang, J. G. Zhang, J. Liu, *Sci. Rep.* **2013**, *3*, 3130.
[6] J. Xiao, X. Zhang, H. Fan, Q. Lin, L. Pan, H. Liu, Y. Su, X. Li, Y. Su, S. Ren, Y. Lin, Y. Zhang, *Adv. Energy Mater.* **2022**, *12*, 2202602.
[7] R. Horia, D. Nguyen, A. Y. S. Eng, Z. W. Seh, *Batte.r Supercaps.* **2022**, *5*, 202200011.
[8] Y. Sun, Y. Wang, L. Jiang, D. Dong, W. Wang, J. Fan, Y. C. Lu, *Energy Environ. Sci.* **2022**, *16*, 265.
[9] W. Zhao, Z. Pan, Y. Zhang, Y. Liu, H. Dou, Y. Shi, Z. Zuo, B. Zhang, J. Chen, X. Zhao, X. Yang, *Angew. Chem., Int. Ed.* **2022**, *61*, 2205187.
[10] M. Salama, I. Shterenberg, H. Gizbar, N. N. Eliaz, M. Kosa, K. Keinan-Adamsky, M. Afri, L. J. W. Shimon, H. E. Gottlieb, D. T. Major, Y. Gofer, D. Aurbach, *J. Phys. Chem. C* **2016**, *120*, 19586.
[11] S. B. Son, T. Gao, S. P. Harvey, K. X. Steirer, A. Stokes, A. Norman, C. Wang, A. Cresce, K. Xu, C. Ban, *Nat. Chem.* **2018**, *10*, 532.
[12] Q. Zhao, S. Stalin, L. A. Archer, *Joule* **2021**, *5*, 1119.
[13] R. Lv, X. Guan, J. Zhang, Y. Xia, J. Luo, *Natl. Sci. Rev.* **2020**, *7*, 333.
[14] Z. Liang, C. Ban, *Angew. Chem., Int. Ed.* **2021**, *60*, 11036.
[15] S. Hou, X. Ji, K. Gaskell, P. F. Wang, L. Wang, J. Xu, R. Sun, O. Borodin, C. Wang, *Science* **2021**, *374*, 172.
[16] F. Wang, H. Hua, D. Wu, J. Li, Y. Xu, X. Nie, Y. Zhuang, J. Zeng, J. Zhao, *ACS Energy Lett.* **2023**, *8*, 780.
[17] D. T. Nguyen, A. Y. S. Eng, M. F. Ng, V. Kumar, Z. Sofer, A. D. Handoko, G. S. Subramanian, Z. W. Seh, *Cell. Rep. Phys. Sci.* **2020**, *1*, 100265.
[18] Y. Dong, S. Di, F. Zhang, X. Bian, Y. Wang, J. Xu, L. Wang, F. Cheng, N. Zhang, *J. Mater. Chem. A Mater.* **2020**, *8*, 3252.
[19] L. Ma, J. Vatamanu, N. T. Hahn, T. P. Pollard, O. Borodin, V. Petkov, M. A. Schroeder, Y. Ren, M. S. Ding, C. Luo, J. L. Allen, C. Wang, K. Xu, *Proc. Natl. Acad. Sci. U A* **2022**, *119*, e2121138119.
[20] I. Gunasekara, S. Mukerjee, E. J. Plichta, M. A. Hendrickson, K. M. Abraham, *J. Electrochem. Soc.* **2015**, *162*, A1055.
[21] Z. Li, H. Rao, R. Atwi, B. M. Sivakumar, B. Gwalani, S. Gray, K. S. Han, T. A. Everett, T. A. Ajantiwalay, V. Murugesan, N. N. Rajput, V. G. Pol, *Nat. Commun.* **2023**, *14*, 868.
[22] K. Xu, *Chem. Rev.* **2004**, *104*, 4303.
[23] A. Webber, *J. Electrochem. Soc.* **1991**, *138*, 2586.
[24] R. Attias, B. Dlugatch, O. Blumen, K. Shwartsman, M. Salama, N. Shpigel, D. Sharon, *ACS Appl. Mater. Interfaces* **2022**, *14*, 30952.
[25] W. Hu, Y. Peng, Y. Wei, Y. Yang, *J. Phys. Chem. C* **2023**, *127*, 4465.
[26] C. Combellas, F. Kanoufi, A. Thiébault, *J. Electroanal. Chem.* **2001**, *499*, 144.
[27] H. Zhang, Z. Li, W. Xu, Y. Chen, X. Ji, M. M. Lerner, *Nanotechnology* **2018**, *29*, 325402.
[28] V. Otieno-Alego, G. A. Hope, H. J. Flitt'i, D. P. Schweinsberg, The Effect Of Hydroquinone And Methoxypropylamine On The Pitting Corrosion Behaviour Of A-470 Low Alloy Turbine Disc Steel **1993**.

[29] V. Prabhakaran, G. Agarwal, J. D. Howard, S. Wi, V. Shutthanandan, D. T. Nguyen, L. Soule, G. E. Johnson, Y. S. Liu, F. Yang, X. Feng, J. Guo, K. Hankins, L. A. Curtiss, K. T. Mueller, R. S. Assary, V. Murugesan, *ACS Appl. Mater. Interfaces* **2023**, *15*, 7518.
[30] M. J. Michalczyk, *Organometallics* **1992**, *11*, 2307.
[31] D. T. Nguyen, A. Yong Sheng Eng, M. F. Ng, A. D. Handoko, G. Sandhya Subramanian, Z. Wei Seh, *Cell Rep Phys Sci* **2020**, *1*, 100265.
[32] D. Banfi, L. Patiny, *Chimia (Aarau)* **2008**, *62*, 280.
[33] A. M. Castillo, L. Patiny, J. Wist, *J. Magn. Reson.* **2011**, *209*, 123.
[34] J. Aires-de-Sousa, M. C. Hemmer, J. Gasteiger, *Anal. Chem.* **2002**, *74*, 80.
[35] A. K. Rappe, C. J. Casewit, K. S. Colwell, W. A. Goddard, W. M. Skiff, *J. Am. Chem. Soc.* **1992**, *114*, 10024.
[36] S. Grimme, C. Bannwarth, P. Shushkov, *J. Chem. Theory Comput.* **2017**, *13*, 1989.
[37] C. Lee, W. Yang, R. G. Parr, *Phys. Rev. B* **1988**, *37*, 785.
[38] A. D. Becke, *Phys. Rev. A* **1988**, *38*, 3098.
[39] S. Grimme, J. Antony, S. Ehrlich, H. Krieg, *J. Chem. Phys.* **2010**, *132*, 154104.
[40] M. Franchini, P. H. T. Philipsen, L. Visscher, *J. Comput. Chem.* **2013**, *34*, 1819.
[41] Y. P. Li, J. Gomes, S. Mallikarjun Sharada, A. T. Bell, M. Head-Gordon, *J. Phys. Chem. C* **2015**, *119*, 1840.
[42] S. Grimme, *Chem. – Eur. J.* **2012**, *18*, 9955.
[43] A. Kramida, Y. Ralchenko, J. Reader, N. I. S. T. A. S. D. Team, National Institute of Standards and Technology, Gaithersburg, MD **2022**.
[44] I. Weber, J. Ingenmey, J. Schnaidt, B. Kirchner, R. J. Behm, *ChemElectroChem* **2021**, *8*, 390.
[45] C. R. Herd, D. Smith, N. G. Adams, *Int. J. Mass Spectrom. Ion Proc.* **1989**, *91*, 177.